

**Supporting information**

On the Electrochemical Degradation of Pt-Ni  
Nanocatalysts: An Identical Location Aberration-  
Corrected STEM Study

*Somaye Rasouli, Deborah Myers, Nancy Kariuki, Kenji Higashida, Naotoshi Nakashima, Paulo Ferreira\**

S. Rasouli

Materials Science and Engineering Program, University of Texas at Austin, Austin, Texas,  
78712, USA

Dr. D. Myers

Chemical Sciences and Engineering Division, Argonne National Laboratory, Lemont, Illinois,  
60439, USA

Dr. N. Kariuki

Chemical Sciences and Engineering Division, Argonne National Laboratory, Lemont, Illinois,  
60439, USA

Prof. K. Higashida

Department of Materials Science and Engineering, Kyushu University, now at National Institute  
of technology, Sasebo College, Sasebo, 857-1193, Japan

Prof. N. Nakashima

Department of Applied Chemistry & WPI-I2CNER, Kyushu University, Fukuoka, 819-0395,  
Japan

Prof. P.J. Ferreira

Materials Science and Engineering Program, University of Texas at Austin, Austin, Texas, 78712, USA

International Iberian Nanotechnology Laboratory, Braga, Portugal

Mechanical Engineering Department and IDMEC, Instituto Superior Técnico, University of Lisbon, Av. Rovisco Pais, 1049-001 Lisboa, Portugal

Email: ferreira@mail.utexas.edu

### Characterization of the Initial Powder

In order to analyze the effect of potential cycling on PtNi NPs, a complete characterization of the initial powder is required. The PtNi powder used for this study has an average equivalent particle diameter of 5.8 nm with a distribution of particles ranging from 3 to 12 nm with the majority of the particles lying between 5 to 7 nm (Figure S1).

The majority of NPs exhibit a solid solution of Pt and Ni, as shown by the aberration-corrected HAADF STEM image taken with the beam direction,  $B=[110]$  (Figure S2a). The lack of superlattice reflections (see Fast Fourier Transform (FFT) in the inset of Figure S2a) shows that the NP has a disordered structure, where Pt and Ni are randomly distributed in a FCC crystal structure. However, as noted in Figure S2a, pockets of bright and dark contrast are evident throughout the NP, which is likely due to the heterogeneous distribution of elements. Yet, as the HAADF STEM image contrast is dependent on both thickness and mass, it is important to separate both effects. In this context, the column-by-column normalized HAADF intensity variation across the NP (orange line in Figure S2a) is compared with the normalized thickness variation of a truncated octahedron projected along the same orange line (Figure S2b). For this analysis, the HAADF intensity profile of this particle along the orange line in Figure S2a was measured with Digital Micrograph. Then the intensity profile was scaled linearly to range between 0 and 1. In other

words, the intensity value of each column was normalized with respect to the maximum intensity in the profile according to:

$$I_{Normalized\ i} = \frac{I_i - I_{min}}{I_{max} - I_{min}}$$

where  $I_{Normalized\ i}$  is the normalized intensity of the  $i$ th atomic column,  $I_i$  is the intensity of the  $i$ th atomic column measured by Digital Micrograph,  $I_{max}$  and  $I_{min}$  are the maximum and minimum intensity of the profile, respectively. The minimum intensity was considered to be zero and equal to the HAADF intensity of vacuum.

Since the intensity of the HAADF image is approximately proportional to the square of the atomic number ( $Z^2$ ) and linearly proportional to thickness ( $t$ ) ( $I_{normalized\ i} \propto tZ^2$ ), we can determine the normalized atomic number of each atomic column along the orange line. In this fashion, the normalized atomic number along the orange line was defined as the square root of the ratio of normalized integrated intensity and normalized thickness in Figure S2b. This is shown in Figure S2c and provides us with a quantity to compare the average atomic number of each atomic column. Since the atomic number of Pt is considerably higher than that of Ni ( $Z_{Pt}=78$ ,  $Z_{Ni}=28$ ), it is reasonable to suggest that the regions with brighter contrast are Pt-richer relative to the regions with darker contrast. Thus, the normalized atomic number profiles in Figure S2c indicate the formation of a heterogeneous composition profile where Pt-richer regions (brighter) with higher atomic number, and Ni richer regions (darker) with lower atomic numbers are observed.

Although most of the NPs exhibit a solid solution structure, there are NPs which show partially ordered structures, as shown in Figure S3. In this image, the super-lattice reflections present in the FFT of the blue square 1 verifies the ordered structure of this region, while the lack of super-lattice

reflection in the FFT of square 2 shows a disordered structure. In fact, the atomic structure of the ordered region matches well the HAADF STEM computer simulation of the  $L_{10}$  structure viewed along the 111 zone axis (Figure S3b) which is the stable structure for 50% Pt-50% Ni according to the Pt-Ni phase diagram.<sup>1</sup>

The EDS mapping of the NPs confirms a Pt rich layer on their surface, as well as small Pt rich and Ni rich regions inside the particles (Figure S4). This is consistent with the intensity variations in the HAADF image shown in Figure S2. An important observation from the composition distribution of the NPs is that smaller particles have a considerably higher amount of Pt and a thicker Pt-rich shell (compare particle 1 and 2 in Figure S4d). The reason for this behavior starts with the leaching process of Ni, the less noble element, which occurs preferentially at the outermost layers of the NP, leading to the formation of a Pt-rich surface. In smaller NPs, the fraction of surface atoms with respect to bulk atoms increases, and thus smaller NPs are more prone to Ni leaching due to the higher density of low coordination surface sites, such as steps and kinks. This results in the formation of a thicker Pt-rich layer and higher Pt/Ni ratio in these particles.<sup>2-5</sup>

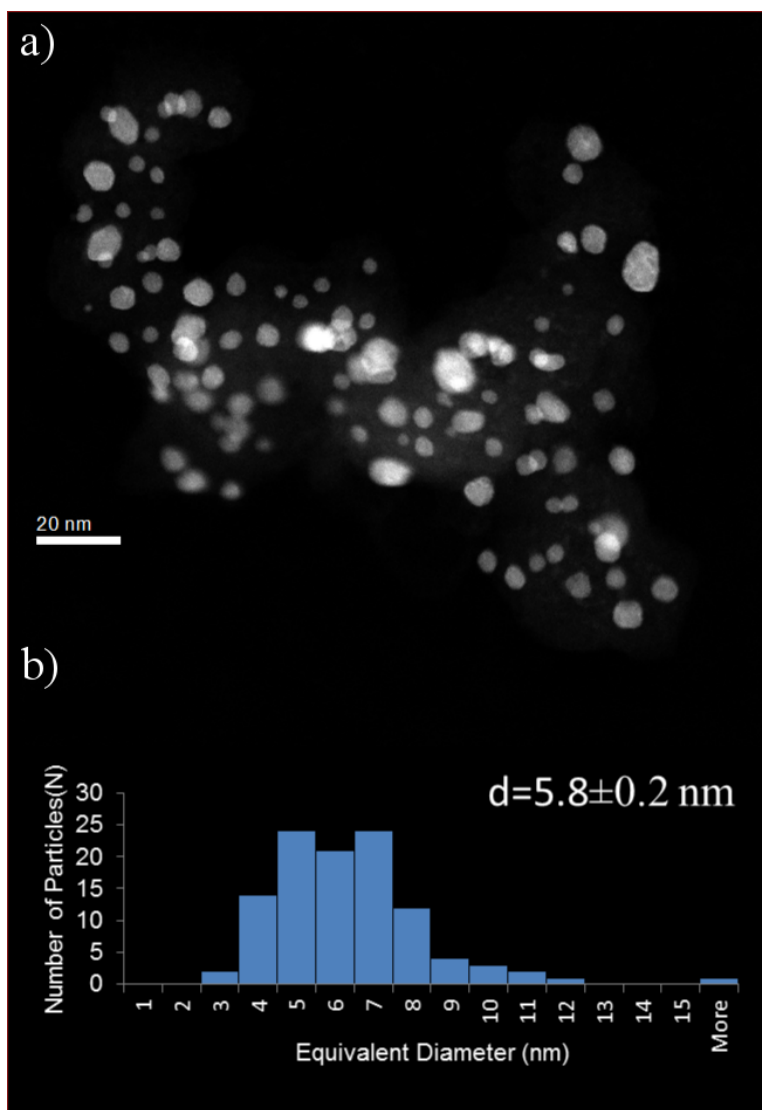
There are other particles, mostly larger than 10 nm, showing high variations in contrast (Figure S5). EDS mapping and the corresponding average intensity of the Pt and Ni signals, along the blue rectangle in the HAADF image, confirms the formation of large Pt-rich and Pt-poor regions within the NPs, as well as nano-sized pores. The EDS mapping of the particle in Figure S5 contains regions where the signals from both Pt and Ni exhibit a very low intensity. This is further confirmed from the intensity profiles of Pt and Ni along the blue rectangle (inset of Figure S5), where the intensities of Pt and Ni decrease significantly. Overall, these regions represent parts of the nanoparticle that suffered significant dissolution and lead to the formation of nano-sized pores.

The presence of nano-pores is only seen in the larger NPs. This is confirmed by kinetic Monte Carlo simulations, which show that the amount of porosity is proportional to  $1/r$ .<sup>6</sup> In other words, the formation of pores is initiated faster in larger particles, rather than in smaller ones, due to the fact that the higher dissolution rate in smaller particles leads to the dissolution of Ni from greater depths into the particle, which results in thicker Pt-rich shells. Subsequently, when a thick Pt-rich shell forms on the surface of these particles, this acts as a passivating layer protecting the underlying Ni from further dissolution and thus restricting pore formation.<sup>7-12</sup> As shown by EDS mapping, the Pt-rich layer also exists on the surface of larger particles, but it is thinner than that of smaller particles.

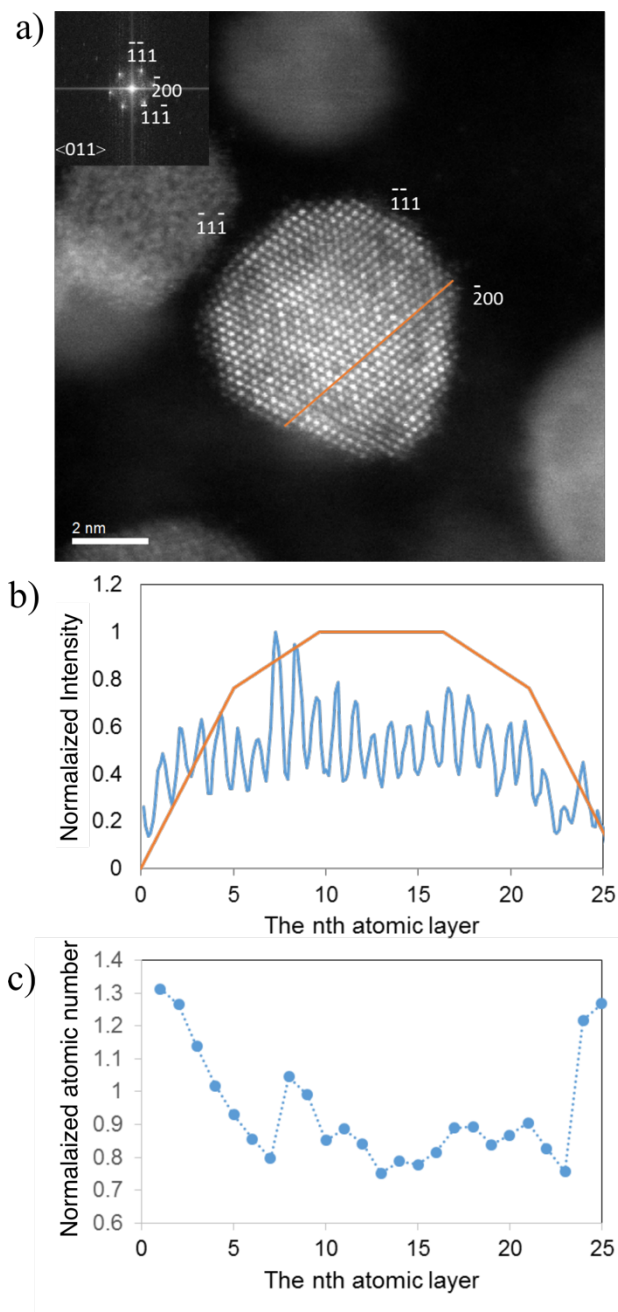
ORR mass activity and area specific activity were measured before cycling and after 2000 and 7000 cycles, as shown in table S1. Both the mass and area specific activity decreased significantly after just 2000 cycles. This can be attributed to the loss of the influence of Ni on the lattice spacing of the surface Pt. After 7000 cycles, the mass and area specific activities increased relative to that measured after 2000 cycles. A possible source of this increase is a growth in particle size according to the well-known particle size dependence of ORR<sup>13</sup>. Cyclic voltammetry curves are shown in Figure S7.

Table S1. Mass activity and specific activity of the NPs before and after potential cycling

<b>Number of Cycles</b>	<b>Mass Activity (mA/mg-Pt)</b>	<b>Specific Activity (mA/cm<sup>2</sup>)</b>
0	625	1260
2000	206	412
7000	278	588



**Figure S1.** a) HAADF STEM image of the Pt-Ni NPs, and b) Particle size distribution of the Pt-Ni NPs.



**Figure S2.** a) Aberration-corrected HAADF image of a Pt-Ni NP and corresponding FFT (inset).  
 b) Normalized intensity across the NP and c) Normalized atomic number for each atomic column  
 across the NP (along the orange line).

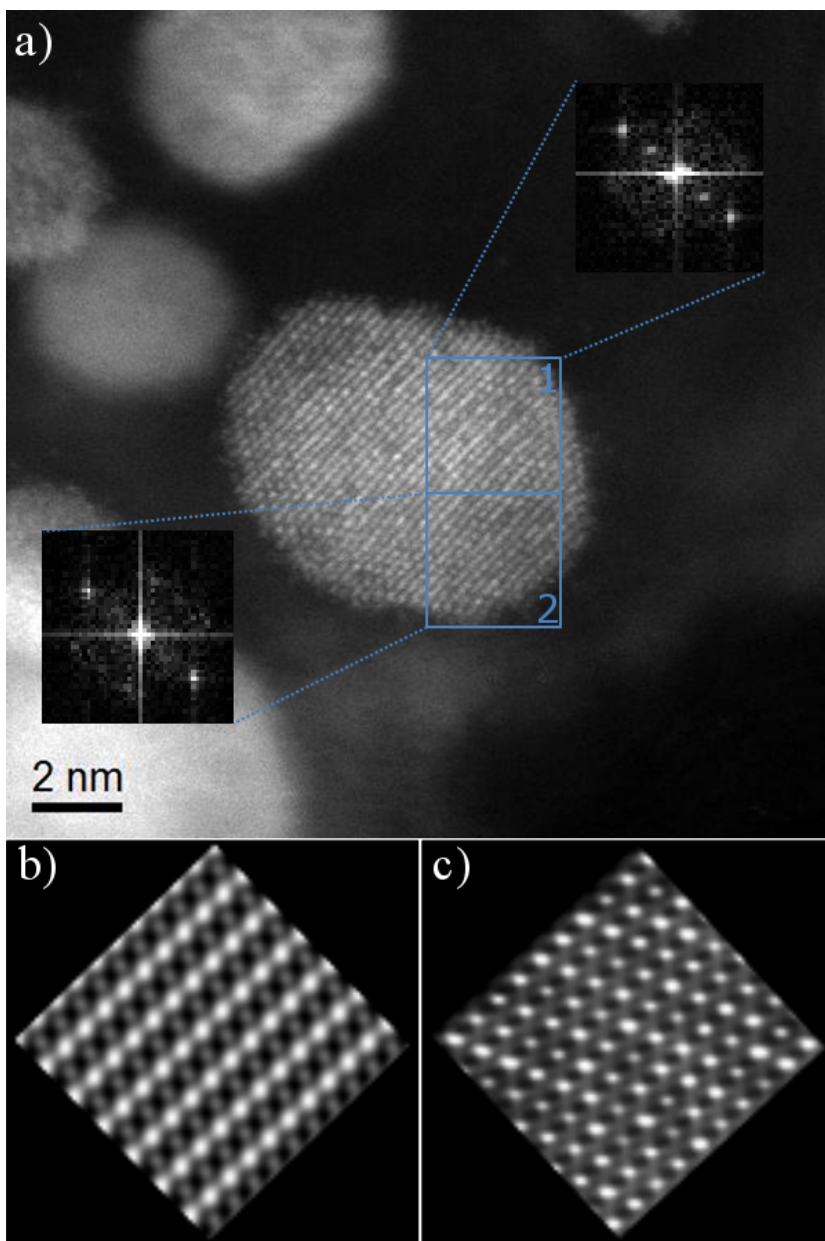


**Figure S3.** a) Aberration-corrected HAADF STEM image of a Pt-Ni NP. The insets show the FFTs of regions 1 and 2 within the NP, b) STEM HAADF computer simulation of the  $L_{10}$  structure (space group  $P4/mmm$ ) along the  $\langle 111 \rangle$  zone axis corresponding to region 1, and c) STEM HAADF computer simulation of a random solid solution (space group  $Fm\bar{3}m$ ), corresponding to region 2.

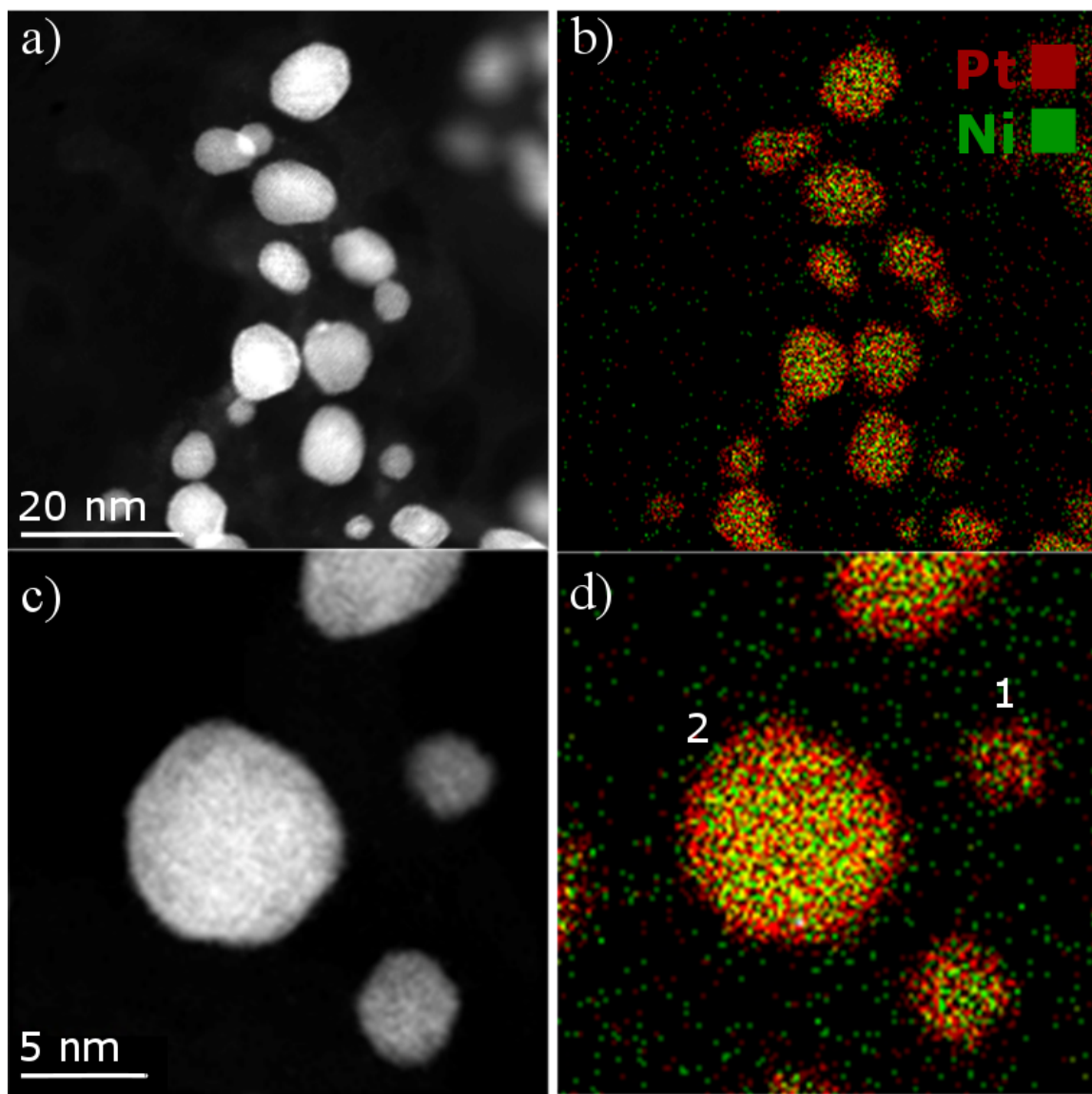


**Figure S4.** a) HAADF STEM of Pt-Ni NPs, b) EDS mapping of the NPs in a), c) higher magnification HAADF STEM image of the Pt-Ni NPs, and d) EDS mapping of the NPs in c) showing a Pt-rich surface layer on the NPs.

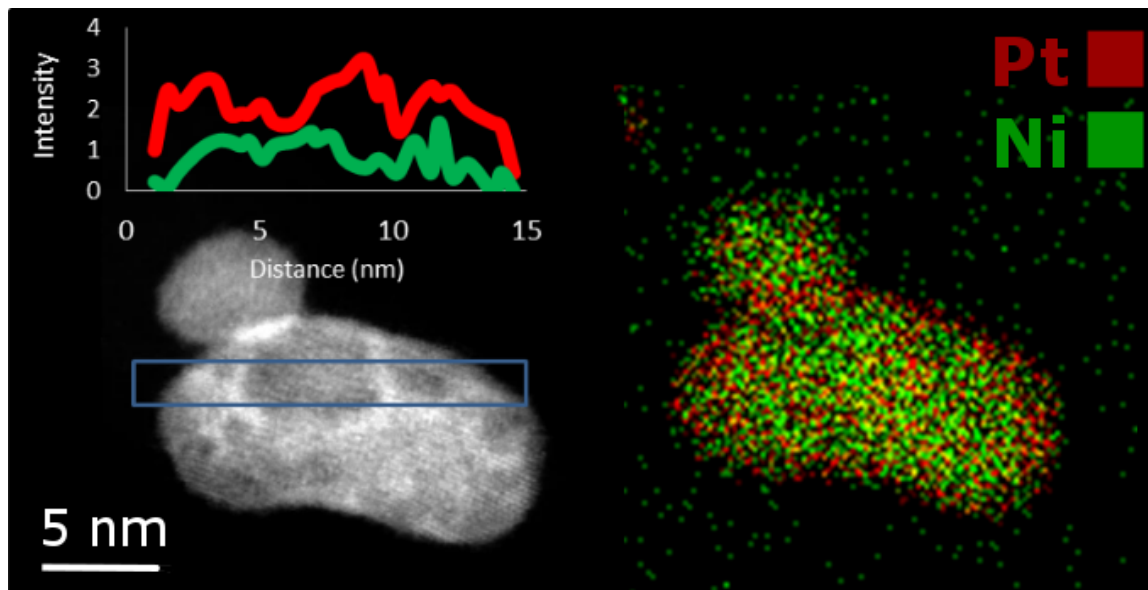


**Figure S5.** HAADF STEM image and EDS mapping of large Pt-Ni NPs (>10 nm). The inset shows the intensity profile of Pt and Ni along the blue rectangle.

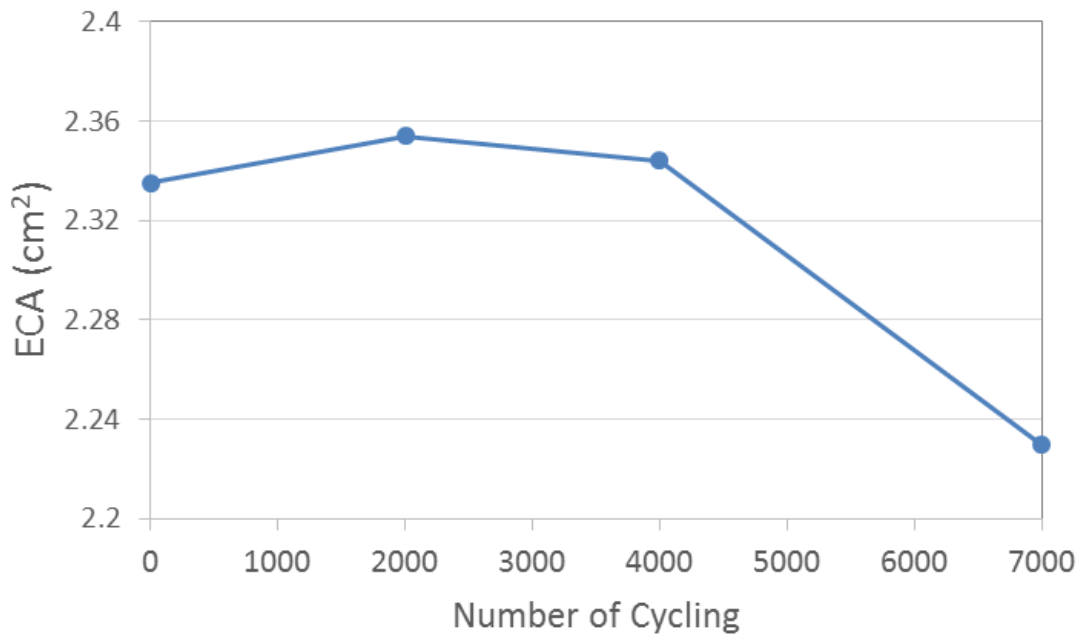


**Figure S6.** ECA loss of the PtNi NPs at different stages of potential cycling.

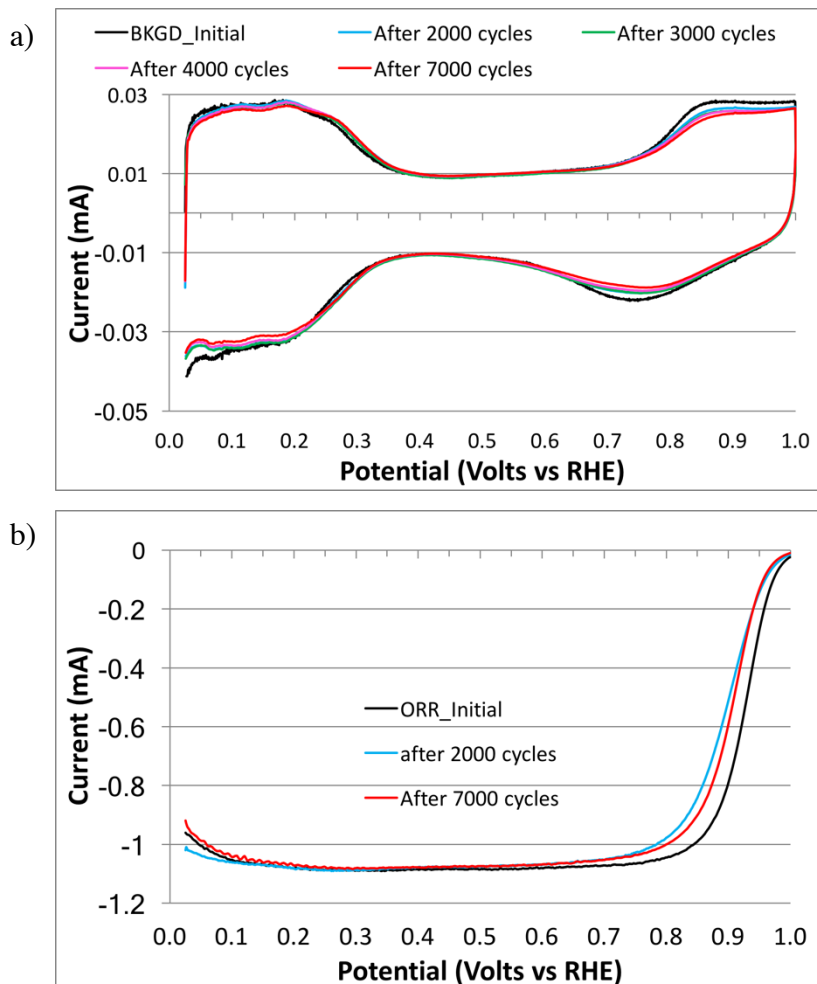


Figure S7. a) Background cyclic voltammograms taken at a scan rate of  $10 \text{ mV s}^{-1}$  of PtNi/C in deaerated  $0.1 \text{ M HClO}_4$  electrolyte as a function of number of accelerated stress test potential cycles between  $0.6$  and  $1.1 \text{ V}$  at  $500 \text{ mV/s}$ . b) Oxygen reduction reaction linear sweep voltammograms from  $0.025 \text{ V}$  to  $1.0 \text{ V}$  at  $10 \text{ mVs}^{-1}$  of PtNi/C on a rotating disk electrode (RDE) as a function of number of accelerated stress test cycles.  $\text{O}_2$ -saturated  $0.1 \text{ M HClO}_4$  electrolyte. RDE rotation rate:  $1600 \text{ rpm}$ .

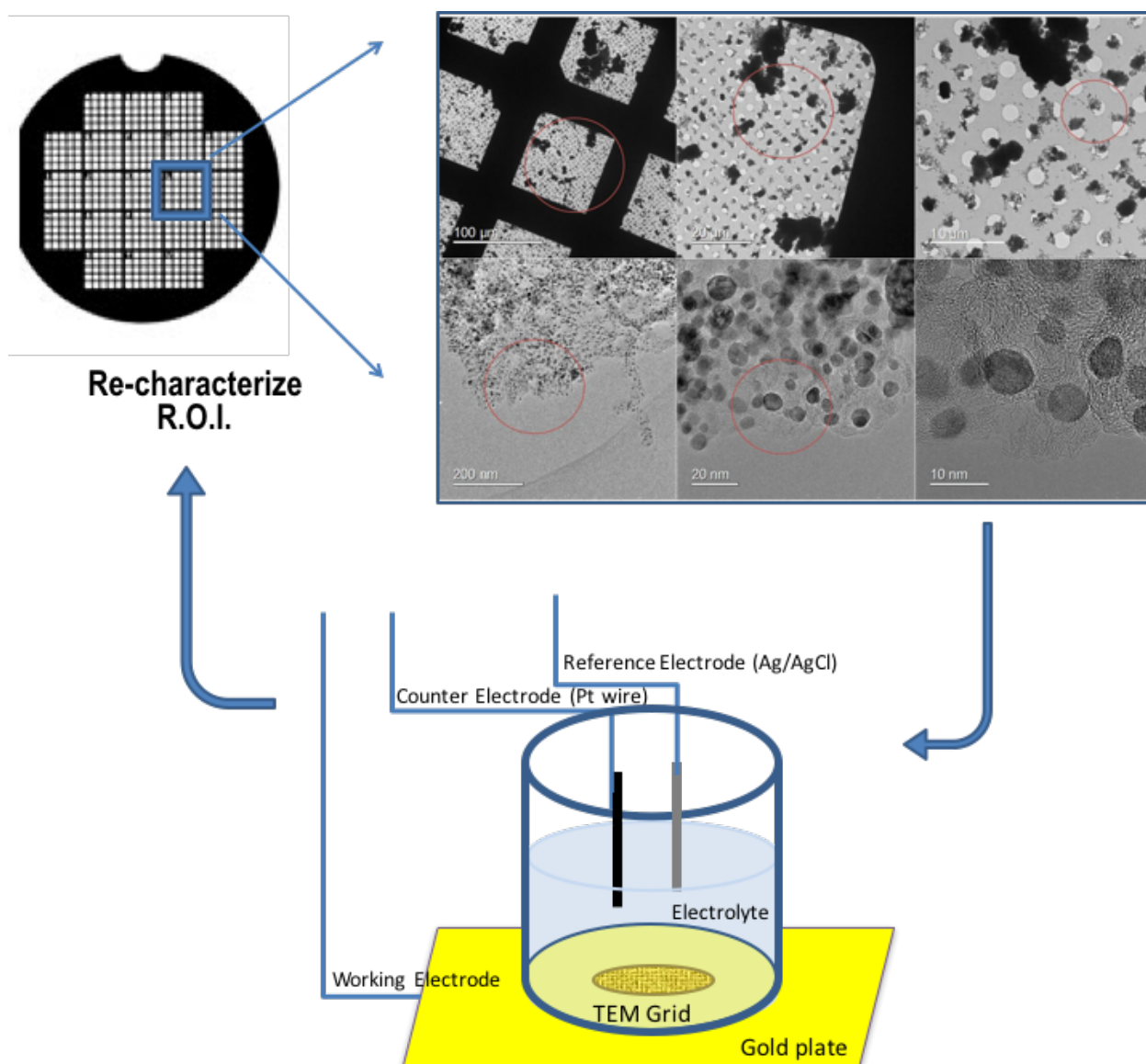


Figure S8. Schematic of identical location TEM procedure

## References

- (1) Baker, H.; Okamoto, H. ASM Handbook. *ASM Int.* **1992**.
- (2) Chen, S.; Gasteiger, H. A.; Hayakawa, K.; Tada, T.; Shao-Horn, Y. P. *J. Electrochem. Soc.* **2010**, *157* (1), A82.
- (3) Chen, S.; Sheng, W.; Yabuuchi, N.; Ferreira, P. J.; Allard, L. F.; Shao-Horn, Y. *J. Phys. Chem. C.* **2008**, *113*, 1109–1125.
- (4) Watanabe, M.; Tsurumi, K.; Mizukami, T.; Nakamura, T.; Stonehart, and P. Activity and Stability of Ordered and Disordered Co/Pt Alloys for Phosphoric Acid Fuel Cells. *J. Electrochem. Soc.* **1994**, *141*, 2659.
- (5) Snyder, R. C.; Doherty, M. F. *J.* **2007**, *53* (5), 1337–1348.
- (6) McCue, I.; Snyder, J.; Li, X.; Chen, Q.; Sieradzki, K.; Erlebacher, J. *Phys. Rev. Lett.* **2012**, *108* (22), 225503.
- (7) Snyder, J.; McCue, I.; Livi, K.; Erlebacher, J. *J. Am. Chem. Soc.* **2012**, *134* (20), 8633–8645.
- (8) Oezaslan, M.; Heggen, M.; Strasser, P. *J. Am. Chem. Soc.* **2012**, *134* (1), 514–524.
- (9) Li, X.; Chen, Q.; McCue, I.; Snyder, J.; Crozier, P.; Erlebacher, J.; Sieradzki, K. *Nano Lett.* **2014**, *14* (5), 2569–2577.
- (10) Jeyabharathi, C.; Hodnik, N.; Baldizzone, C.; Meier, J. C.; Heggen, M.; Phani, K. L. N.; Bele, M.; Zorko, M.; Hocevar, S.; Mayrhofer, K. J. *J. ChemCatChem* **2013**, *5* (9), 2627–

2635.

- (11) Oezaslan, M.; Hasché, F.; Strasser, P. *J. Phys. Chem. Lett.* **2013**, *4* (19), 3273–3291.
- (12) Baldizzone, C.; Gan, L.; Hodnik, N.; Keeley, G. P.; Kostka, A.; Heggen, M.; Strasser, P.; Mayrhofer, K. J. J. *ACS Catal.* **2015**, *5* (9), 5000–5007.
- (13) Gasteiger, H. A.; Kocha, S. S.; Sompalli, B.; Wagner, F. T. *Appl. Catal.* **2005**, *56* (1–2), 9–35.